Structure of Aqueous Pluronics Films: Dynamics of Surface Directed Mesophase Formation

G. J. A. Sevink* and J. G. E. M. Fraaije

Leiden Institute of Chemistry (LIC 7), Gorlaeus Laboratories, P.O. Box 9502,
2300 KA Leiden, The Netherlands

H. P. Huinink

Department of Applied Physics, Eindhoven University of Technology, P.O. Box 513,
5600 MB Eindhoven, The Netherlands

Received August 7, 2000; Revised Manuscript Received July 3, 2001

ABSTRACT: The dynamic mean-field density functional method is used to describe copolymer phase separation in a slit. The confined system consists of a mixture of 55% flexible triblock poly(ethylene oxide) (PEO)−poly(propylene oxide) (PPO)−poly(ethylene oxide) (PEO) copolymer (trade name Pluronics) and 45% solvent. The triblock under consideration, Pluronics L64 $(EO)_{13}(PO)_{30}(EO)_{13}$, is modeled as a Gaussian chain. In bulk the copolymer forms a hexagonally packed array of PO-rich cylinders, embedded in a EO-rich matrix. This is the first three-dimensional calculation and study of a specific triblock in a confined regime. In particular, by choosing the dynamic density functional (DDFT) method for this theoretical studies, the morphology is a result of a dynamic pathway during the phase separation. As such, this study goes beyond an investigation of the stability of predefined morphologies. It is shown that, for the special case of wall−water energetic interactions equal to EO−wall interactions, the phase diagram for the triblock copolymer resembles the phase diagram for confined asymmetric diblocks without water. For this case, the effect of the presence of water is very subtle and influences the features of the morphologies only locally. Starting with a very thin slit and increasing the slit width, parallel (with respect to the plates) oriented cylindrical phases are most frequent, but transition regions of perpendicular cylinders for intermediate slit widths are observed. We also find morphologies that are not present in films of asymmetric diblock copolymers, such as micelles and rodlike particles. An important observation is that, as in the asymmetric diblock case, the influence of the surface on the *orientational* order is present through the whole sample, whereas the influence of the surface on the morphology *type* is limited to the vicinity of the surface. However, because of the difference in chain architecture and the presence of water, the latter region is shown to be larger than in the diblock case.

1. Introduction

The physics behind the formation of microstructures in block copolymers has been investigated extensively in the past three decades. From a scientific point of view these materials are interesting, because order−disorder transitions can be studied under relatively simple experimental conditions and can form a large variety of sometimes very complex microstructures. Materials that exhibit these microstructures are commercially also very interesting because they influence and are able to improve the mechanical properties of materials, both in bulk and at contact boundaries.

Typical examples of copolymers of industrial interest are polystyrene−polybutadiene (PS−PB or PS−PB−PS) and poly(ethylene oxide)−poly(propylene oxide) (PEO−PPO or PEO−PPO−PEO) block copolymers. The first are widely applied in bitumen for roofing and road applications and as tougheners. For the second type of copolymer, Schmolka[1] reports over 1000 articles on the applications in the medical and pharmaceutical industries alone. They play a fundamental role in biology and are widely applied because of their ability to self-organize at interfaces and in solution and thus modify interfacial properties and enhance compatibility or partition. Their tendency to self-assembly stems from the fact that the PO is relatively hydrophobic, whereas the EO blocks are relatively hydrophilic. Quite an amount of work (both theoretically and experimentally) for this class of amphiphilic block copolymers has been done by groups in Lund: self-assembly in solution,[2−4] phase behavior in aqueous solution,[5−8] and absorption at solid interfaces.[9−11] In this article we will focus on one member of this Pluronics family, namely Pluronic L64 $(EO)_{13}(PO)_{30}(EO)_{13}$.

Studies on the behavior of PEO−PPO−PEO triblocks in confined regimes focus on the surface activity and surface adsorption (see summary in ref 12). The surface activity reflects the ability of the copolymer to reduce the surface tension of water. Surface adsorption relates to the tendency for solute to concentrate at the air−water interface.[13] This is determined by measuring the surface tension as a function of the bulk concentration, often at different temperatures.

The determination of a phase diagram in the presence of solid surfaces is, to our knowledge, not carried out to an extent that may be expected because of their industrial relevance. Confinement plays an important role in the mesoscale morphology formation since, in diblock and triblock copolymer thin films,[14−22] the surface properties of these materials, such as adhesion, friction, and wetting, are controlled by the mesostructures near the surface. From experiments with diblocks and triblock films, it is well-known that confinement influences the phase behavior to a considerable extent.

Most of the work on thin films has been done on symmetric diblock copolymer melts. The behavior of these copolymers has been studied systematically by

---

* Corresponding author.

10.1021/ma001378k CCC: $22.00

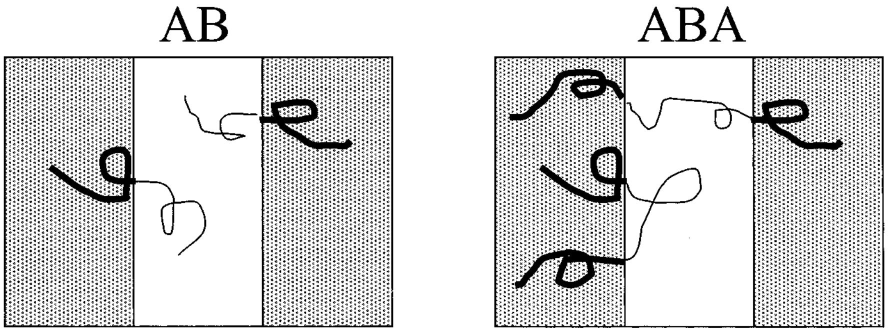

Figure 1. Chain conformations in AB diblock and ABA triblock copolymers. Only one type of interface exists in AB diblock and ABA triblock copolymers. ABA triblocks can form either bridges or loops.

experiments and theory.[23,24] As in the bulk, lamellae are formed. The basic finding of all these studies was that the orientation of the lamellae depends on both the wetting properties of the blocks and the thickness of the confined system. Strong preferential wetting by one of the blocks favors a parallel orientation of the lamellae. Deviations of the bulk lamellar spacing due to the film thickness favors a perpendicular orientation. One should emphasize that the latter effect is only observable in confined systems, which cannot adjust their thickness. Otherwise, terraces are formed. Little work has been done on films of cylinder-forming asymmetric block copolymers.[19,25−27] However, in a recent theoretical study[27] we have shown that these polymers behave more or less similar as their symmetric counterparts. The cylinders orient parallel when one of the blocks preferentially wets the film surfaces. The perpendicular orientation is preferred when the domain spacing is frustrated by the thickness of the film. Differences were also predicted. It was found that transitions to noncylindrical morphologies could be induced by the surfaces. At certain combinations of film thicknesses and surface−polymer interactions, lamellae and catenoid−lamellae (perforated lamellae) were predicted.

Until quite recently, the experimental focus was mainly directed to diblock copolymer films. Experiments for triblock copolymers in thin films were few,[15,28,29] and extrapolation of results obtained by AFM at the surface into the film was sometimes found to be difficult. Recently, a method was developed[32] to image the volume of ultrathin films, by using a scanning force microscope combined with stepwise erosion in a radio-frequency plasma. This method was applied to image ultrathin poly(styrene-*b*-butadiene-*b*-styrene) triblock copolymer films. It was observed that the structure underlying the “observable” surface patterns cannot simply be extrapolated to three dimensions.

Although many triblock copolymer films are prepared by swelling in solvents, a rigorous analysis of the phase behavior as a function of slit width and surface interactions for an aqueous triblock copolymer film is still missing. It was experimentally found that the presence of solvent has effects on the mesostructures in thin films.[30] We want to use the (dynamic) mean-field density functional theory to construct a theoretical phase diagram for a specific ABA triblock copolymer with solvent in a slit. Since the parameters space is four-dimensional (slit width and interaction parameters for three components), it is computationally not feasible to scan the whole phase diagram. In view of the absence of experimental data, only “generic” features will be demonstrated. The method for investigating the dynamic formation of mesostructures was developed by our group.[33] In the past 3 years, progress has been made with studying the effect of processing conditions like applied shear, reactions, and geometry constraints. In contrast to traditional schemes of polymer phase separation where a Landau Hamiltonian is used with vertex functions calculated in the random phase approximation, we numerically calculate the detailed free energy F of polymer systems using the path integral formalism. The benefit of this approach is that it avoids the truncation of the free energy and therefore represents, for example, metastable states more accurately.

The method used here was validated by determining bulk morphologies of a system of aqueous triblock polymer surfactants—Pluronics L64 $(EO)_{13}(PO)_{30}(EO)_{13}$.[35] The polymer is represented by a Gaussian chain $E_3P_9E_3$ (where E and P are statistical units or beads) and the solvent by S. The parametrization is rather cumbersome and involves comparison of different structure factors for single chains and determination of Flory−Huggins (FH) parameters by extrapolation of vapor pressure data and group contributions.[35] The parametrization is well-defined as is shown by the determination of the bulk morphologies of 4R25 $(PO)_{19}(EO)_{33}(PO)_{19}$ (so-called inverse Pluronics, modeled as $P_6E_8P_6$) for the same set of interaction parameters. The simulation results show good correspondence with experiments for both triblock copolymers for different percentages of polymer surfactants in an aqueous solution.[35]

By simulating phase separation in an aqueous solution of triblock copolymer PL64 in a confined regime, we touch upon three new aspects: (i) We consider a triblock instead of a diblock copolymer.[27] Although ABA triblocks self-assemble into morphologies similar to diblocks, their chain conformation is very different (Figure 1). (ii) We consider a triblock copolymer solution instead of a triblock copolymer melt. It is well-known that three bead systems exhibit different phase behavior due the existence of one extra degree of freedom (the presence of water). (iii) We use a specific experimental system, namely PL64. For the aqueous solutions of PL64 in bulk, a large number of microstructures were found depending on the presence of water: micellar (50% water), hexagonal (45%), bicontinuous (40%), and lamellar (30%) phases.[5] Since we want to restrict our attention to the effect of confinement, we consider a 55% aqueous solution of Pluronics PL64 in a slit. As mentioned, this percentage of polymer concentration corresponds to a hexagonally packed cylindrical phase for PL64.[5] Application of shear on this system influences the orientation of the phase[37] but does not change the nature of the phase. In contrast, a solution of 60% PL64 shows a breakdown of the bicontinuous morphology to a coexistent hexagonal/lamellar phase under the influence of shear.[36] Considering the 55% PL64 system allows us to investigate the changes in the morphology due to the effect of confinement and surface interactions only, without any bias of metastable states of the system itself.

Our setup is a slit geometry with solid plates at both sides (same setup as in Huinink[27]). This system simulates an experimental setup of a confined or flat film. In most of the experimental setups films are considered that are unconfined on one side. These films can adjust their geometry due to the presence of air. Experimental tools such as TappingMode atomic force microscopy can be employed to find the true sample surface.[31] In the case of SBS films, it was found that conventional TM-AFM height images reflect lateral differences of tip indention and that the surface was in reality completely flat. However, even in the case of terrace formation, we can qualitatively deduce results for free films from our simulations for confined films, by a simple method described in our article for confined diblock films.[27]

In the remainder, we will first give a short overview of the dynamic density functional theory in the confined case. In our simulations, there exists a complex interplay between four independent variables: three energetic wall interaction variables and the slit width H. To directly compare our results with experiments, we need energetic Flory−Huggins (FH) interaction parameters for the interaction between the surface and the different blocks of the triblock copolymer. Since we do not have experimental values, we choose to consider three different cases: neutral, hydrophilic, and hydrophobic surfaces. First, we will consider the influence of the slit width H on the morphologies for a slightly and stronger hydrophilic substrate (and equal solvent−wall and EO−wall interactions). Second, we will employ the extra degree of freedom and deviate the hydrophobic interactions between the wall and the EO and solvent for some specific slit widths. In short, we consider neutral (with respect to all species) and hydrophobic surfaces. We finalize the simulation part by comparing our findings to results for asymmetric diblock copolymer films in detail. Although experimental validation of our simulation results is out of the scope of this article, we propose a setup for experimental validation in the conclusions.

2. Method

2.1. Theory. The polymer melt is modeled as a slightly compressible system, consisting of Gaussian chain molecules in a mean-field environment. We will give a short overview for completeness. More details can be found in earlier publications.[33,34] The free energy functional for copolymer melts has a form that is similar to the free energy that is used in[33,35,38]

$$
\begin{aligned}
F[\{\rho\}] &= F^{\mathrm{id}}[\{\rho\}] + F^{\mathrm{nid}}[\{\rho\}] \\
&= -kT \ln \frac{\Phi^n}{n!} - \sum_I \int_V U_I(\mathbf{r})\, \rho_I(\mathbf{r})\, \mathrm{d}\mathbf{r} + \\
&\quad \frac{1}{2} \sum_{I,J} \int_{V^2} \epsilon_{IJ}(\mathbf{r} - \mathbf{r}')\, \rho_I(\mathbf{r})\, \rho_J(\mathbf{r}')\, \mathrm{d}\mathbf{r}\, \mathrm{d}\mathbf{r}' + \\
&\quad \frac{1}{2} \sum_I \int_{V^2} \epsilon_{IM}(\mathbf{r} - \mathbf{r}')\, \rho_I(\mathbf{r})\, \rho_M(\mathbf{r}')\, \mathrm{d}\mathbf{r}\, \mathrm{d}\mathbf{r}' + \\
&\quad \frac{\kappa_H}{2} \int_V \Big(\sum_I \nu_I (\rho_I(\mathbf{r}) - \rho_I^0)\Big)^2 \mathrm{d}\mathbf{r} \qquad (1)
\end{aligned}
$$

except for the fourth term that contributes only in the direct vicinity of a solid object, which is, in our case, a plane. This term accounts for the interaction of a polymer melt with surfaces. In this equation, n is the number of polymer molecules, I is a component index, ρ_I are the density fields of the different bead types I, and V is the system volume. The intramolecular partition function Φ for ideal Gaussian chains in an external potential field U can be calculated as a path integral over all bead positions.[33] The density is given by

$$
\rho_I[U](r) = \frac{n}{\Lambda^{3N}} \sum_{s=1}^{N} \delta_{Is} \int_{V^N} \psi(R_s)\, \delta(r - R_s) \prod_{s=1}^{N} \mathrm{d}R_s \qquad (2)
$$

where Λ is a normalization factor, δ_{Is} is one when s is of species I and zero if not, R_s is the positions of the sth bead, and

$$
\psi(R_s) = \frac{1}{\Phi} \mathrm{e}^{-\beta[H^{\mathrm{G}} + \sum_{s=1}^{N} U_s(R_s)]} \qquad (3)
$$

with H^{G} a Gaussian chain Hamiltonian.[33] Since there is a bijective relation between the external potential fields U and the density fields ρ,[33] a pair of fields (ρ, U) uniquely defines a free energy value $F[\rho,U]$. Inside the object, the densities ρ_I of the different bead types are equal to zero. The plates have fixed positions and occupy a subset V^0 of the total simulation volume V. The constant density field ρ_M (M denoting the slit surface density type) that appears in eq 1 is defined as $\rho_M(\mathbf{r}) = 1$ for $\mathbf{r} \in V^0$ and $\rho_M(\mathbf{r}) = 0$ for $\mathbf{r} \in V/V^0$. The average concentration is ρ_I^0 and ν_I is the particle volume. The cohesive interactions have kernels $\epsilon_{IJ}(|\mathbf{r} - \mathbf{r}'|) = \epsilon_{IJ}^0(3/2\pi a^2)^{3/2} \exp((-3/2a^2)(\mathbf{r} - \mathbf{r}')^2)$. The surface interactions ϵ_{IM} have similar kernels. The Helfand compressibility parameter is κ_{H}.[38] We minimize the free energy of eq 1 by means of a system of partial differential equations, describing the time evolution of the system. The time evolution of the density field $\rho_I(\mathbf{r})$ can be described by a time-dependent Landau−Ginzburg equation[39,40]

$$
\frac{\partial \rho_I}{\partial t} = M_I \nabla \cdot \rho_I \nabla \frac{\delta F}{\delta \rho_I} + \eta_I \qquad (4)
$$

Here $\mu_I = \delta F/\delta\rho_I$ is the intrinsic chemical potential, M_I is the mobility, and η_I is the stochastic noise which is distributed according to the fluctuation−dissipation theorem.[41] As a kinetic model, we have chosen a local exchange mechanism. The free energy is minimized in this way in order to incorporate the dynamics of the phase separation.

Periodic boundary conditions are employed in all three Cartesian directions. For the diffusion flux in the vicinity of the filler particles, rigid-wall boundary conditions are used. A simple way to implement these boundary conditions in accordance with the conservation law is to allow no flux through the slit surfaces, i.e.

$$
\nabla \mu_I \cdot \mathbf{n} = 0 \qquad (5)
$$

where $\mathbf{n}$ is the normal pointing toward the filler particle. The rigid-wall boundary conditions also apply to the noise η_I. The noise may have a uniform or Gaussian distribution with moments dictated by the fluctuation−

dissipation theorem and is equal to[41] (in the notation of that article)

$$\eta_I(\mathbf{r},t) = \sqrt{\frac{2}{\beta}}\nabla_{\mathrm{r}}\cdot\sqrt{M_I\rho(\mathbf{r})}\,w_{\mathrm{K}}(\mathbf{r},t) \tag{6}$$

where w_{K}^c (c indicates x, y, or z) is a completely decorrelated random field with uniform or Gaussian distribution

$$\langle w_I^c(r,t)\rangle = 0$$

$$\langle w_I^c(r,t)\; w_J^{c'}(r',t')\rangle = \delta_{IJ}\delta_{cc'}\delta(r-r')\;\delta(t-t') \tag{7}$$

The special correlation of the noise ensures that the time integration of the Langevin eq 4 generates a Boltzmann ensemble of density fields (for details see refs 33 and 41). In our case, uniform noise was used.

2.2. Computational Procedure. A Crank−Nicolson scheme is used for the numerical integration of eq 4. The starting configurations for the time integration are homogeneous density distributions $\rho_I = \rho_I^0$ and the external field $U = 0$. Notice that the starting conditions for the U are fixed upon a constant. The time integration is carried out as long as the driving chemical potential is present. The time process is monitored with the help of an order parameter P,

$$P_I(t) = \frac{\nu^2}{V}\sum_I\int_V(\rho_I{}^2(r) - (\rho_I^0)^2)\;\mathrm{d}r \tag{8}$$

At $t = 0$, P_I equals zero for all I. If P_I levels off to a constant value, the system has reached an equilibrium or is trapped in a metastable state. Even if the system is in a (meta)stable state, it is continuously challenged by fluctuations created by the noise. It has to be remarked that the parameter P cannot be used to describe the stability of the morphologies. It is only a measure for the grade of demixing of unlike beads and is by definition insensitive to morphological transitions, which do not involve significant changes in the grade of demixing. Therefore, we have used P together with a direct evaluation of the density fields. It is important to notice that even when no dynamic changes are observed in the density fields, it is still possible that the system has not reached a global or local equilibrium. This could be the case when the time scales of the dynamics are beyond the time scale, covered by our simulations. In a strict sense, the observed “equilibrium” morphologies therefore rather generate a morphology diagram than a phase diagram.

3. Results and Discussion

Here we simulate the behavior of a Pluronics L64 polymer. For all simulations, a three-dimensional cubic grid (with grid spacing h) of dimension $L \times W \times L$ is used, where $L = 32$. At all boundaries we employ periodic boundary conditions. In the box, a infinitely long plate is placed orthogonal to the y-dimension (at $y = h$) of one grid cell thick. Since we have periodic boundary conditions in the y direction as well, this means that the variable $H = (W - 1)h$ denotes the width of the slit. We have chosen such a value of L by considering other simulations:[35] the boundary conditions do not affect the isotropy of the structure factor in the unconfined case, and the computational effort for the large number of phase points that we want to consider is within our limits. For the remainder, all dimensions are given in terms of grid points unless mentioned differently.

In comparing our results directly to experiments, we observe a number of difficulties. First, in experiments often films are used that are in contact with air instead of slits/confined films. To compare our results qualitatively to these experiments, we would have to include free surfaces in our simulation setup. This is necessary since some features, such as formation of terraces, cannot be represented within our current approach. We note that from our results some qualitative results for free films can be calculated.[27] Second, determination of FH parameters for the wall−polymer and wall−solvent interactions is not always feasible in experiments. For the wall, we think of hydrophobically modified silica surfaces or air, such as present in thin soap films. In the latter case, air would behave as a hydrophobic surface. Some experimental tools are available for the determination of the interaction parameters, such as surface force measurements or AFM (atomic force microscope) experiments with colloidal particles attached to the tip. However, at this moment there are no experiments to compare our simulation results with. Therefore, our interest is the generic behavior. In this section we will use different values for the surface interaction parameters and consider the results qualitatively and compare them with our results for diblocks, where we have some experimental validation.

As mentioned in the Introduction, the PL64 molecule is modeled as a $E_3P_9E_3$ Gaussian chain. The solvent is modeled as a single bead S. The P part is relatively hydrophobic, whereas the E part is relatively hydrophilic. In the system, we have three exchange parameters for the interbead interactions: $\chi_{IJ} = (\beta/2\nu)[\epsilon_{IJ}^0 + \epsilon_{JI}^0 - \epsilon_{JJ}^0 - \epsilon_{II}^0]$ ($I \in \{\mathrm{E, P, S}\}$) and three for the interaction with the surfaces χ_{IM}. The normal interaction parameters were calculated from vapor pressure data using a Flory−Huggins expression and determined to be $\chi_{\mathrm{ES}} = 1.4$ and $\chi_{\mathrm{PS}} = 1.7$. The parameter χ_{EP} is determined by group contribution methods[44] as 3.0. The surface related interaction parameters χ_{EM}, χ_{PM}, and χ_{SM} are chosen different in the different simulations in order to mimic different (weak) hydrophobic, neutral, or (weak) hydrophilic surfaces. The values we have chosen are shown schematically in Figure 2.

We focus on a 55% polymer concentration. For the unconfined case, the experimentally found phase is a hexagonally packed cylindrical phase.[5] The theoretical findings for our set of parameters are in good agreement with these experiments.[35] It is shown in a later article that external factors such as applied shear do not change the nature of the morphology but have a big effect on the orientation of the structures.[37] From these earlier calculation in the presence of shear, we have found the repeat distances between the hexagonally packed cylinders to be between 6 and 7 grid cells.

The parameters that are used in the numerics are dimensionless and chosen similar to the ones used in earlier work.[35] For simplicity, we use identical mobility coefficients M and bead volume ν for all components. The volume fraction $\theta_I = \nu\rho_I$ is integrated numerically on an equidistant Cartesian grid, with mesh size $h = 1.3$ nm, by a Crank−Nicolson scheme. The dimensionless variables are (see refs 33 and 35 for details and discussions): the dimensionless time step $\Delta\tau =$

Table 1. Morphologies Characterized as a Function of *H* for $\chi_{EM} = 1.0$, $\chi_{PM} = 0.0$, and $\chi_{SM} = 1.0$[a]

label	H	phase	$y = \tau/\Delta\tau$	label	H	phase	$y = \tau/\Delta\tau$
a	5	wetting	4000	k	15	$C_\perp$	4000
b	6	wetting	4000	l	16	$C_{\parallel,2}$	8000
c	7	wetting	4000	m	17	$C_{\parallel,2}$	8000
d	8	$L_{\parallel,1}$	4000	n	18	$C_{\parallel,2}$	8000
e	9	$C_\perp$	4000	o	19	$C_{\parallel,2}$	4000
f	10	$C_\perp$	8000	p	20	$C_\perp$	8000
g	11	$C_{\parallel,1}$	4000	q	21	$C_{\parallel,3}$	10000
h	12	$C_{\parallel,1}$	4000	r	22	$C_{\parallel,3}$	8000
i	13	$C_{\parallel,1}$	8000	s	31	$C_{\parallel,4}$	4000
j	14	$L_\perp$	10000				

[a] Here, L denotes lamellae and C cylinders.

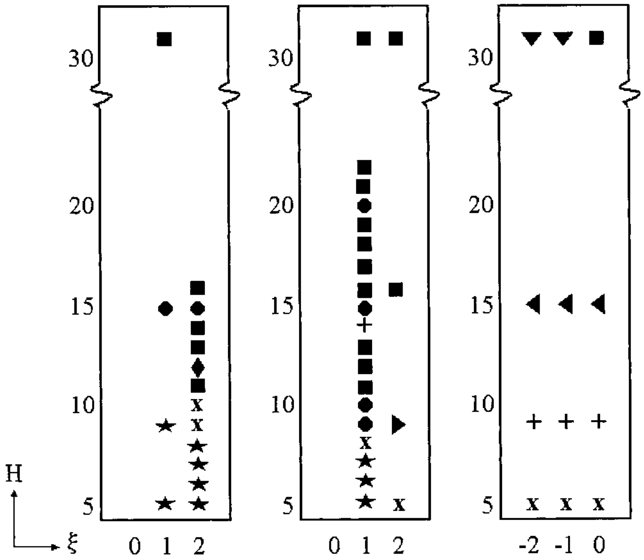

Figure 2. Slices through the phase space (slit width *H* vs $\xi(= \chi_{EM} - \chi_{PM})$) that are considered in this article. The slices are for constant values of χ_{SM}: 2.0 (left), 1.0 (middle), and 0.0 (right). Each point is represented by its P morphology: no structure (★), imperfect orthogonal structures (△ pointing left), micellar (△ pointing right), perpendicular lamellar (+), parallel lamellar (×), perpendicular cylindrical (○), parallel cylindrical (□), catenoid (◇), and mixed catenoid and parallel cylindrical (▽).

$\beta^{-1}Mh^{-2}\Delta t = 0.5$ and a grid parameter $d = ah^{-1} = 1.1543$, which gives us an optimal value for the bond length a.[45] The noise scaling parameter $\Omega = \nu^{-1}h^3 = 100$, which can be seen as the number of statistical elements per grid cell (see also refs 33 and 41 for more details). The compressibility parameter $\kappa' = \beta\kappa_H\nu = 10.0$.

3.1. Effect of Interaction. a. Hydrophobic Substrates/Varying *H*. First, we investigate the effect of the slit width *H* for a slightly hydrophobic substrate. The surface related interaction parameters are now chosen equal to $\chi_{EM} = 1.0$, $\chi_{PM} = 0.0$, and $\chi_{SM} = 1.0$ (all in kT). We refer to this choice as case I. For these values, we consider the morphology as a function of the slit distance *H*, ranging from $H = 5$ to 22 grid points, which is a range between 6.5 and 28.6 nm (for $h = 1.3$ nm). To see the behavior for thicker films, we have also performed simulations for $H = 31$ (40.3 nm). Table 1 contains all the results, and Figure 3 shows some representative morphologies.

For the smallest slit size ($H = 5$), we observe wetting of the surfaces by a *P*-rich layer (Figure 3a). Since this *P*-rich layer is always present in simulations in this part of the phase diagram, we do not mention the presence of this layer in the remainder.

Increasing the value of *H*, we remain in the domain of $L_\parallel$ until $H = 9$, where the morphologies change to a hexagonally packed $C_\perp$ (perpendicular cylinders) type of morphology (Figure 3e). For $H = 10$, this perpendicular cylindrical phase remains. The number of time iterations to obtain a perfect structure is much higher, indicating that the system is close to a transition region.

From $H = 11$ to 13, the parallel orientation appears again. The middle layer consists of a cylindrical instead of a lamellar phase. One may conclude from this that the influence of the surface on the *orientational* order is present through the whole sample, whereas the influence on the morphology *type* is only limited to the layer next to the surface. This feature is present in all the simulations, except for $H = 14$ (Figure 3j). At $H = 14$ we observe again a parallel orientation at the surfaces and a system of parallel undulated cylinders that becomes a perpendicular orientated lamellar system at larger time scales. The order parameters $P_I(t)$ for $H < 14$ show a monotone increase with almost constant slope and, at later stages, a slow but monotone convergence to limiting values $\tilde{P}_E$, $\tilde{P}_P$, and $\tilde{P}_W$, without intersections of $P_E(t)$, $P_P(t)$, and $P_W(t)$. The behavior at $H = 14$ is completely different: initially, the order parameters have a dip and intersect, after which they intersect again toward their original positions. The $P_I(t)$ start to increase with a large slope and, at later stages, level off to limiting values with intermediate, clearly distinct plateaus values, indicating the breaking up and reorientation of structures. At $H = 15$ (Figure 3k), we again have a perpendicular oriented cylindrical phase between two parallel lamellae at the surfaces.

As a function of *H* we see a repetitive change in the orientation of the cylinders: a mechanism that is known for diblocks.[27] Another general remark is that for larger *H*; the perfect and stable morphology is reached only at larger time scales. At $H = 20$ (Figure 3p), a defect-rich perpendicular orientation is obtained, and it is found that the defects do not disappear at time scales within the simulation scope. The general mechanism is that the system likes to form layers of parallel oriented cylinders. In the *H* region where the system "adds" one layer, there is an intermediate region of perpendicular orientation. At these intermediate regions, the system needs more time to find its optimal conformation. We observe three subsequent steps going from one to three layers. The width of the regions of perpendicular orientation shrinks when going to higher *H*, as may be expected.

Going to higher surface interaction values, we hope to see an effect on the *orientational* ordering. We now consider the same simulations for doubled surface interaction values ($\chi_{EM} = 2.0$, $\chi_{PM} = 0.0$, and $\chi_{SM} = 2.0$ (all in kT)). This set is known as case II. The results

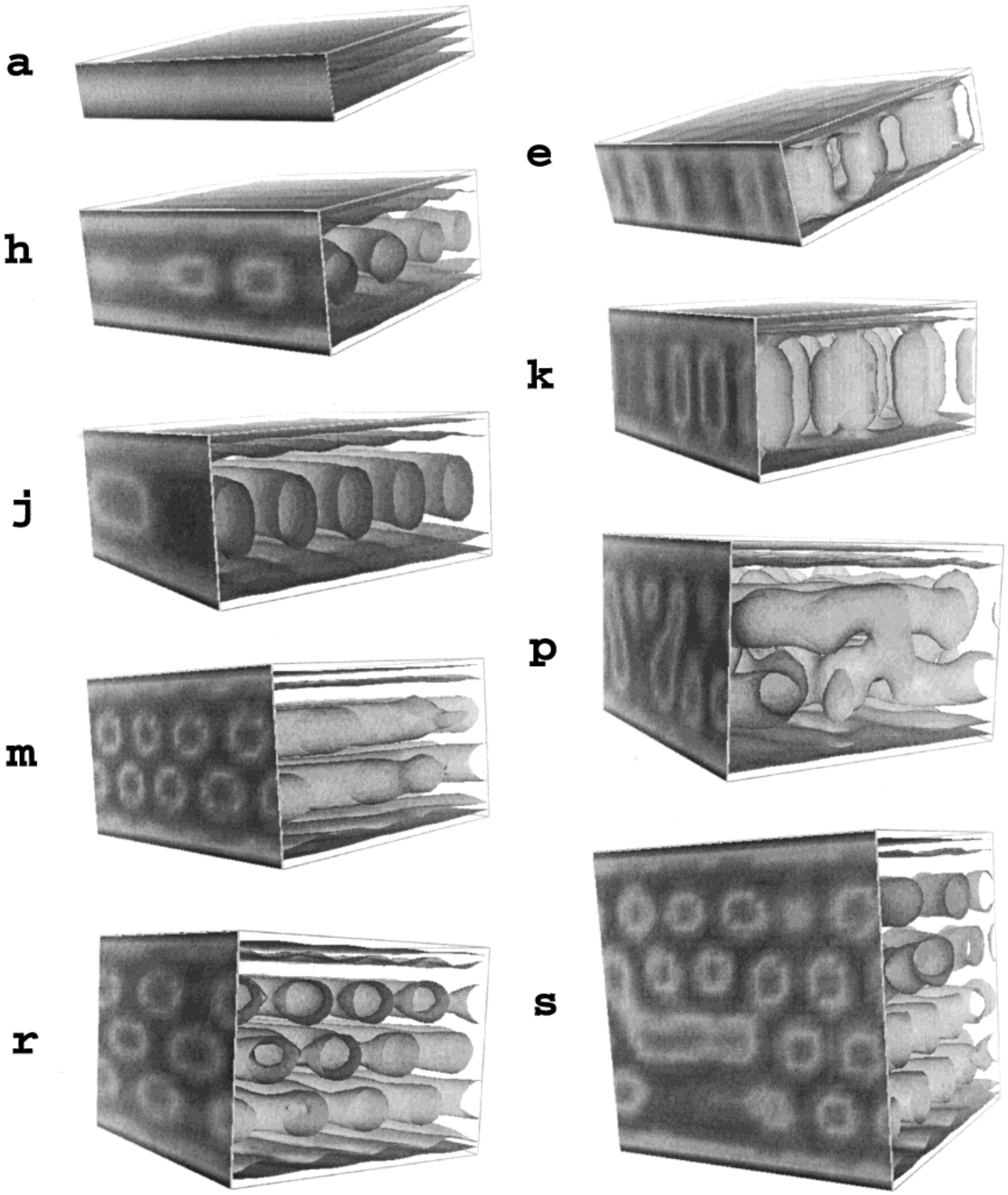

Figure 3. Final morphologies ($\nu\rho_P$ for mean isosurface values) for surface interaction parameters $\chi_{EM} = 1.0$, $\chi_{PM} = 0.0$, and $\chi_{SM} = 1.0$ and different slit widths *H*. The lables reflect the position in Table 1 ($H =$): 5 (a), 9 (e), 12 (h), 14 (j), 15 (k), 17 (m), 20 (p), 22 (r), and 31 (s).

are shown in Table 2 and Figure 4. For $H = 5-8$, we again observe parallel lamellae at the surfaces. At $H = 9$ the perpendicular orientation is absent. Instead, a weak and irregular parallel structure appears in the middle of the box. At $H = 10$ (Figure 4f), a parallel lamella is observed.

At $H = 11$ (Figure 4g) and higher, we observe again an increasing amount of layers of cylindrical phases. For $H = 12$ and $H = 15$ (Figure 4h,k) we found phases that may not be stable. (A discussion will be postponed to the comparison to diblocks.) At $H = 12$, a catenoid phase is found at $y = 2000$ with some defects. At $H = 15$ at the same stage, we find a not yet well developed phase of slightly perpendicular cylinders, residing in two layers. At later stages this reduces to one layer of perpendicular rodlike particles or cylinders. The simulations were continued until $H = 16$ (Figure 4l) and $H = 31$ for a wide slit. For the latter, we have a result similar to the result for smaller surface interactions, be it with more defects (necks). It seems that increasing the surface interactions removes some of the orthogonal structures but increases the formation times of perfect parallel cylindrical structures, evolving from the transition lamellar → catenoid → cylindrical.

b. Variation of Solvent/Substrate Interaction. Having observed the effect of confinement for different values of *H*, we now consider the morphologies as a function of interaction parameters χ_{EM}, χ_{PM}, and χ_{SM} for four specific widths $H = 5$, 9, 15, and 31. The phase points are chosen from the middle of the transitional regions of the phase diagram. Surface wetting by PO is always present.

To see the influence of the specificity of the surface interactions, we have considered two extra cases of

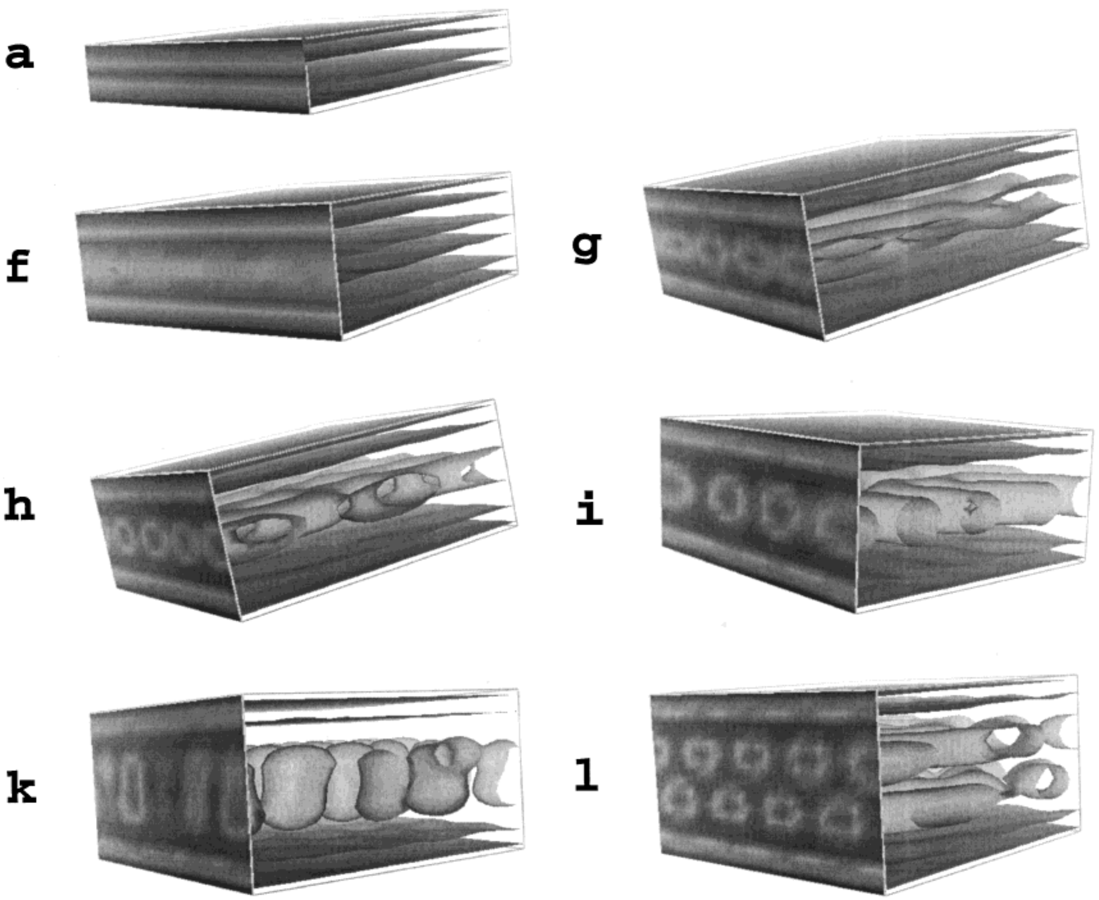

Figure 4. Final morphologies ($\nu\rho_P$ for mean isosurface values) for surface interaction parameters $\chi_{EM} = 2.0$, $\chi_{PM} = 0.0$, and $\chi_{SM} = 2.0$ and different slit widths H. The lables reflect the position in Table 2 (H =): 5 (a), 10 (f), 11 (g), 12 (h), 13 (i), 15 (k), and 16 (l).

Table 2. Morphologies Characterized as a Function of H for $\chi_{EM} = 2.0$, $\chi_{PM} = 0.0$, and $\chi_{SM} = 2.0$[a]

label	H	phase	$y = \tau/\Delta\tau$
a	5	wetting	4000
b	6	wetting	4000
c	7	wetting	4000
d	8	wetting	4000
e	9	$L_{\parallel,1}$	4000
f	10	$L_{\parallel,1}$	4000
g	11	$C_{\parallel,1}$	4000
h	12	$CL_{\parallel,1}$	4000
i	13	$C_{\parallel,1}$	4000
j	14	$C_{\parallel,1}$	4000
k	15	$C_{\perp}$	10000
l	16	$C_{\parallel,2}$	4000

[a] Here, L denotes lamellae, C cylinders, and CL a mixed lamellar/catenoid phase.

hydrophobic surface interactions: χ_{EM} (=2 kT) > χ_{SM} (=1 kT) > 0 (to be referenced to as case III) and χ_{SM} (=2 kT) > χ_{EM} (=1 kT) > 0 (case IV) (and $\chi_{PM} = 0$ kT for both cases). The results are shown in Figures 5(III) and 6(IV). The meaning of this interaction value is that for III the repulsion for the EO part is larger than for the solvent component and for IV vice versa. For $H = 5$ (P-wetting at the surface, Figures 5a and 4a) and $H = 31$ ($C_{\parallel,4}$, Figures 5d and 6d), no real differences can be observed between III and IV, be it that in case III the structure for $H = 31$ is more perfect than for case IV, at the same time stage. For $H = 9$ and $H = 15$, the changes are more drastic. For $H = 9$, a hexagonally packed micellar phase with necks to the lamellae (M) is found for case III (Figure 5b). For the same slit width $H = 9$ we see no real structure in the middle of the box for IV (Figure 6b). For $H = 15$, the morphologies are $C_{\parallel,2}$ for III (Figure 5c) and $C_{\perp}$ for IV (Figure 6c). We observe that, for intermediate film thicknesses $H = 9$ up to $H = 15$, the surface interactions and the slit width have a complex interplay. For these H, the range of the surface interactions is such that it influences the morphology throughout the whole box.

We may also compare III and IV to the earlier simulations case I and II, for equal EO–surface and solvent–surface interactions. It is obvious that for $H = 5$ and $H = 31$ the differences are subtle and can be found in the rate of perfectness of the structures at the same time stage. At $H = 9$ already a number of difference can be observed, ranging from $C_{\perp}$ (I), no structure (II), M (III), and again no structure (IV). Close inspection of the densities for the different species for case III (not shown here) shows that the bulk of EO is present in a thin layer parallel to the boundary layer of PO. The water, however, is homogeneously distributed over the whole slit, with a relatively small decrease of the density profile at positions of high PO density. In this case, one could say that the water takes over the role of the EO in the middle of the slit, allowing for a radial increase of the PO rods into micelles. For case I, the EO and water-rich phases coincide, with high values of both density profiles in perpendicular structures starting at the boundary of the parallel PO-rich layers. For this case the water is mainly present in the EO phase. The PO rodlike structures are separated from the parallel PO boundary–lamellae by a EO/water layer of relatively

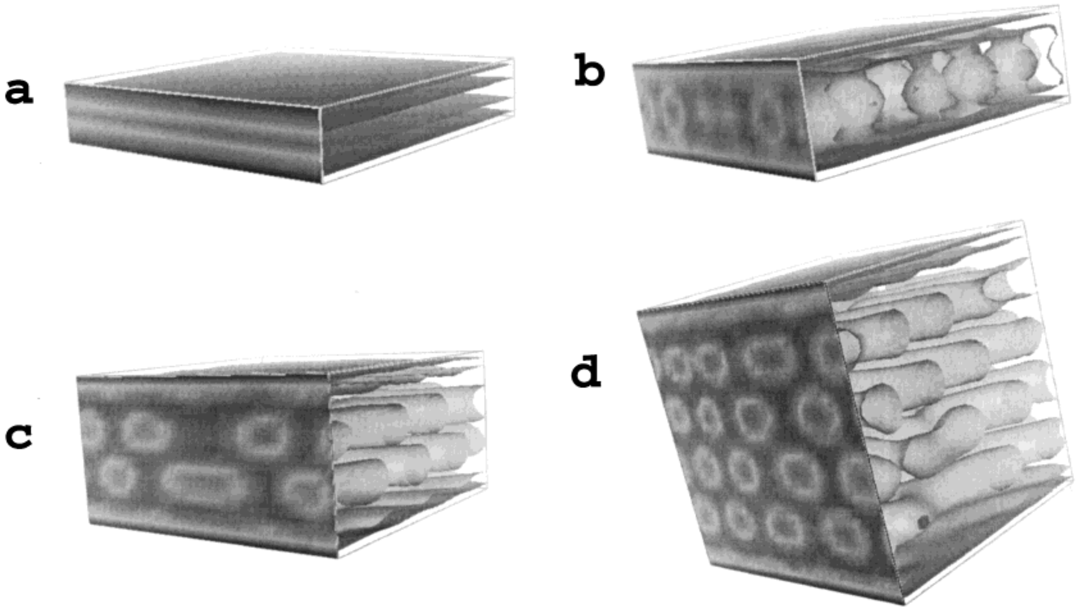

Figure 5. Final morphologies ($\nu\rho_P$ for mean isosurface values) for hydrophobic surface interaction parameters $\chi_{EM} = 2.0$, $\chi_{PM} = 0.0$, and $\chi_{SM} = 1.0$. The results are shown for the slit widths $H = 5$ (a), 9 (b), 15 (c), and 31 (d) and $y = 4000$.

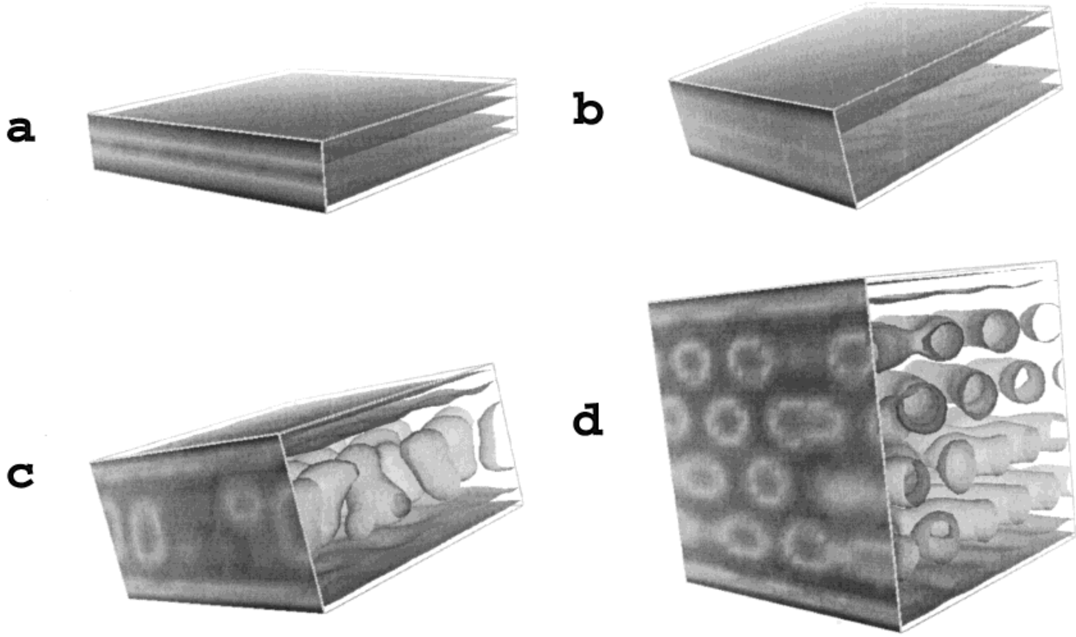

Figure 6. Final morphologies ($\nu\rho_P$ for mean isosurface values) for hydrophobic surface interaction parameters $\chi_{EM} = 1.0$, $\chi_{PM} = 0.0$, and $\chi_{SM} = 2.0$. The results are shown for the slit widths $H = 5$ (a), 9 (b), 15 (c), and 31 (d) and $y = 4000$.

lower density. From these results, we conclude that the triblocks topology and the presence of water affect the perpendicular structures. With increasing repulsive interactions for EO, this block is less likely to be found close to the surface and will be present in a second layer parallel to the wall. It is interesting to see that the EO density also decreases in the middle of the slit. The formation of PO-rich necks to the surface PO layer is entropically unfavorable due to the triblock architecture (see Figure 7; a discussion of this picture is postponed to later in this article). The width of EO/water-rich layer and the amount of phase separation between these two species depend on the degree of repulsion and on the interactions between water, PO, and EO. For increasing χ_{EM} (and constant χ_{SM}) the structure transforms from a slightly undulated cylindrical phase to a micellar phase. Water seems to have an important function: if the disturbance of the balance between the interactions is too strong and the center region of the box is too small to enable structure formation, any structure formation is frustrated. For $H = 15$ we see this behavior in the following structures: $C_\perp$/rodlike (I), $C_\perp$ (II), $L_{\parallel,2}$ (III), and $C_\perp$ (IV). Again the formation of necks is frustrated by higher repulsion of the EO by the surface. For case III, we see similar behavior to the previous slit width $H = 9$: EO-rich thin lamellae are formed parallel to the PO-rich boundary−lamellae. However, the larger slit width allows for the formation of a third thin lamella in the middle of the box. The water is distributed homogeneously, but now with a large decrease of the density profile in PO-rich phases. We find two layers of PO-rich parallel cylinders. In the case of high repulsion of water by the surface (case IV), there is, other than with $H = 9$, enough freedom to form small, distinctly separated

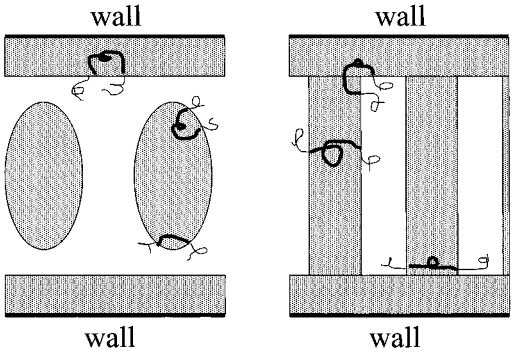

Figure 7. Sketch of the chain conformations for different morphologies. On the left is a side view of the rodlike morphology as is found in our triblock calculations. On the right is a morphology such as found in diblock systems. It is clear from this comparison that the left morphology is entropically more favorable.

layers of perpendicular structures for both EO and PO in the middle of the box. The clear separation of these structures from the boundary PO layers is due to the formation of two thin parallel structures at the boundary PO layers. These thin EO lamellae at the boundary PO layer were not found in case I of equal EO−wall and water−wall interactions. Here, the water/EO phase is homogeneously distributed outside the PO rodlike structures, except for a region in the middle of the slit where a high micellar-like EO region can be observed. Case II is similar to case I, except for the existence of the thin EO lamellae. As a last remark, we observe that the phase boundary for the orthogonal structures is shifted to lower H in the case of III, as can be seen in Figure 2.

c. Hydrophilic Substrates. We have also considered two cases of hydrophilic ($\chi_{EM} = \chi_{SM} = 0$ and $\chi_{PM} > 0$) surfaces interactions: normal ($\chi_{PM} = 1\ kT$) and high ($\chi_{PM} = 2\ kT$) P surface repulsion.

From Figures 8 and 9 (all $y = 4000$) we see that there is no change in morphology due to the different surface interactions whatsoever. For all slit widths, we observe surface wetting by the EO component. At $H = 5$ the PO part is located in a lamella in the middle of the slit. For $H = 9$, perpendicular PO and EO lamellae develop, similar to the case of no interaction (to be discussed later). The rate at which they develop increases with increasing χ_{PM}. For $H = 15$ a structure develops that will eventually form a perpendicular cylindrical $C_\perp$ phase. For $H = 31$ we observe a mixed phase of lamellae and catenoid−lamellae, $CL_\parallel - L_{\parallel,3} - CL_\parallel$, where CL stands for a catenoid phase. Again, we conclude that the range of the surface interaction on the *nature* of the morphology is restricted to only one layer, for large H.

3.2. Effect of Confinement. We investigate the effect of confinement by taking the surface interactions χ_{EM}, χ_{PM}, and χ_{SM} equal to zero. The results can be seen in Figure 10.

Given the cylindrical phase in bulk and the repeat distance for the system under consideration, we expect to find a system of five layers of cylinders for $H = 31$ (Figure 10d), parallel to the plates. An early stage of hexagonal ordering can be observed. At the surface, an E-rich layer can be found due to the entropic preference for small chains at the surface. This shielding layer of E is observed in all simulations where only confinement is concerned. Confinement speeds up the global ordering process: we observe that the formation and orientation of the global structures is at a much smaller time scale than in the unconfined case. For larger H ($H = 79$) this morphology is expected to remain, and indeed we observe 14 layers of cylinders. Because of numerical instability, we had to half the time step $\Delta\tau = 0.25$ to get good numerical behavior. For smaller H the effect of confinement becomes apparent. For $H = 15$ (Figure 10c) an orthogonal orientation can be observed, of cylinders of P-rich material that start to pack in a hexagonal orientation in a matrix of E-material, orthogonal to the plates and E-rich lamellae close and parallel

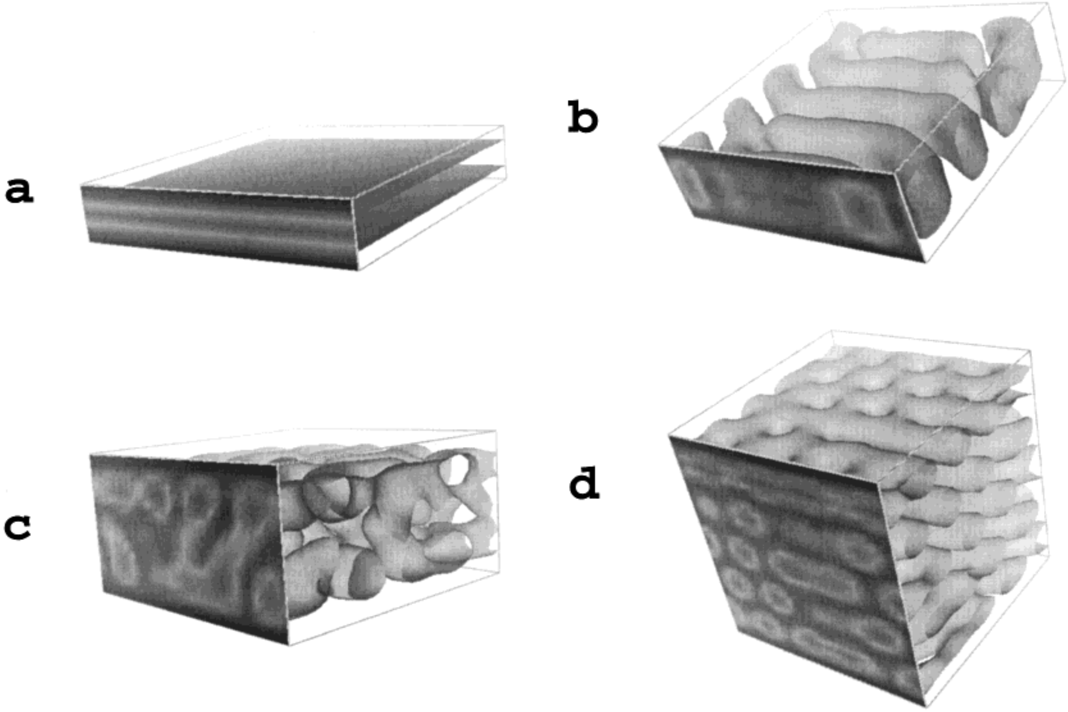

Figure 8. Final morphologies ($\nu\rho_P$ for mean isosurface values) for hydrophilic surface interaction parameters $\chi_{EM} = 0.0$, $\chi_{PM} = 1.0$, and $\chi_{SM} = 0.0$. The results are shown for the slit widths $H = 5$ (a), 9 (b), 15 (c), and 31 (d) and $y = 4000$.

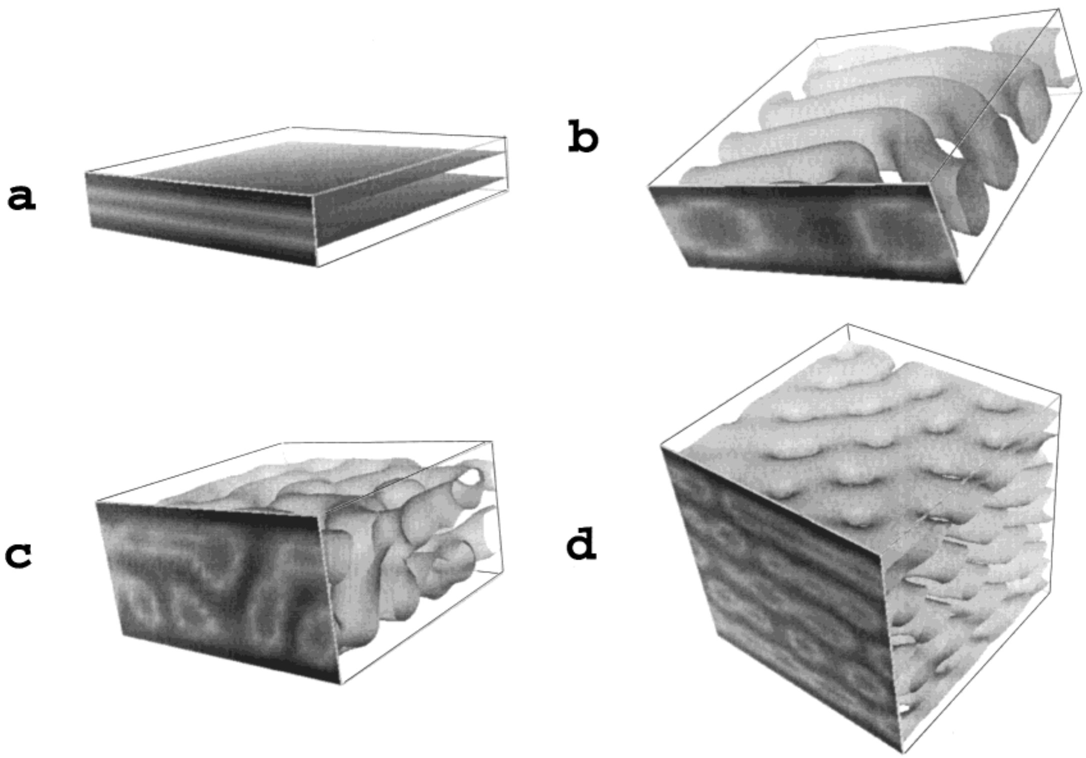

Figure 9. Final morphologies ($\nu\rho_P$ for mean isosurface values) for hydrophobic surface interaction parameters $\chi_{EM} = 0.0$, $\chi_{PM} = 2.0$, and $\chi_{SM} = 0.0$. The results are shown for the slit widths $H = 5$ (a), 9 (b), 15 (c), and 31 (d) and $y = 4000$.

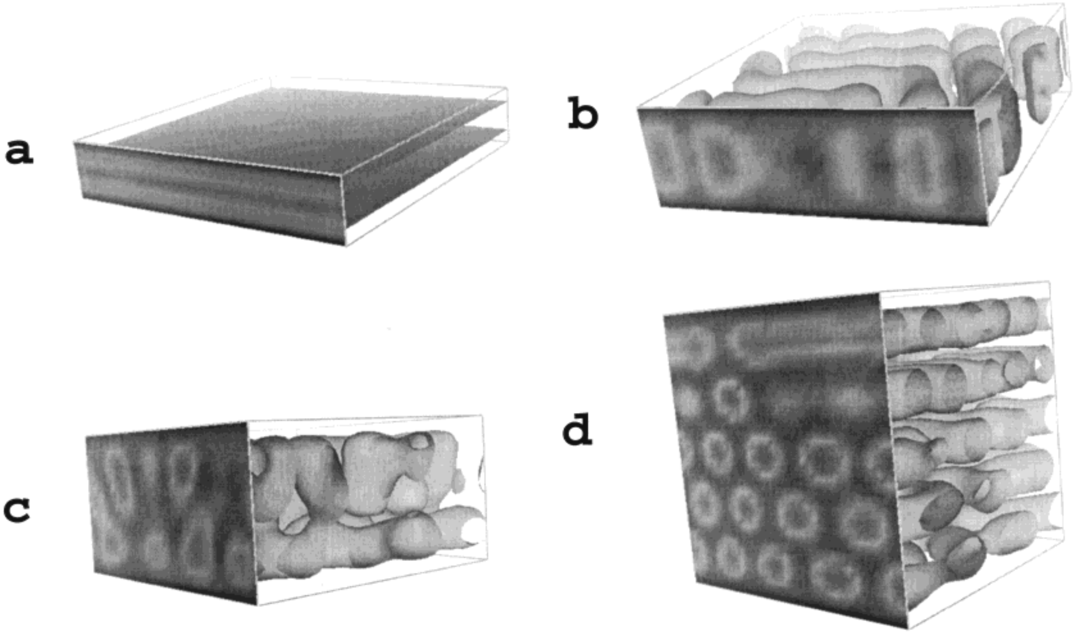

Figure 10. Final morphologies ($\nu\rho_P$ for mean isosurface values) for confinement without surface interactions. The results are shown for the slit widths $H = 5$ (a), 9 (b), 15 (c), and 31 (d) and $y = 4000$.

to the surfaces. For $H = 9$ (Figure 10b) we observe perpendicular lamellae of P-rich material, shielded from the surfaces of the plates by parallel lamellae of E material. Also, perpendicular lamellae of E are observed. If we go to even smaller slits ($H = 5$, Figure 10a), the conformational freedom for the P-rich phase is further decreased and one parallel P lamellae is formed in the middle of the slit.

3.3. Comparison with Asymmetric Diblock Copolymer Films. In general, we conclude that our findings for the aqueous triblock system are very much related to the results for the asymmetric diblock A_3B_6.[27] One important difference is that, in our case, the E part of the $E_3P_9E_3$ is swollen with water and takes the role of the B part of A_3B_6. We compare the phase diagram for the diblocks (as a function of H and $\xi = (\epsilon^0_{AM} - \epsilon^0_{BM})/\nu kT$) of our previous publication[27] and current results for triblocks. Before we do this, we quickly summarize the results for the asymmetric diblock case: increasing ξ from 0.0 to 2.0 leads to morphology changes from mainly parallel with small intermediate perpendicular H-regions ($0 < \xi < 0.5$) (smallest −A− block wets the surface) to perpendicular ($0.5 < \xi < 0.75$)

(transitory phase of no preferential wetting) to mainly parallel with intermediate perpendicular again ($0.75 < \xi < 2.0$) (largest −B− block wets the surface). For higher values of these interaction parameters ξ and some values of H, there is even a transition to catenoid phases. The stability of the latter phase in thin films is investigated by Huinink (private communications). We know that the evolution of structures to cylinders is very quick or takes place via a transformation of lamellae ↔ catenoid phase/perforated lamellae ↔ cylinders. We should keep in mind, however, that there is a region in the phase diagram where the intermediate catenoid phase is stable.

In the triblock case, we see in general similar behavior if we consider the results of the previous subsections. At first glance this may be surprising because of the presence of water that makes these systems seemingly incomparable, but it can be explained. For most of the simulations, the water−wall parameter is not treated as an independent parameter but set equal to the EO−wall interaction. The fact that most of the water resides in the EO phase effectively means that the influence of the water phase on the EO and PO morphology is limited in the case of *equal* interaction of water and E with the walls. This explains the agreement in main features of the considered parts of the phase diagram for diblocks and triblocks.

Although the main features are similar, there are also differences. Close inspection of the old results of Huinink[27] for diblocks revealed the existence of perpendicular lamellae, mistakenly interpreted as cylinders, in the case of $\xi < 0$ (not for $\xi > 0$). However, the micellar and rodlike (in the case of perpendicular orientation) morphologies are not observed for the diblocks. The explanation for the differences is illustrated in Figure 7: it is mainly a consequence of the difference in topology of the diblock vs the triblocks. In the diblock case the perpendicular structures always start at the interface of the wetting lamellae. For triblocks this is not the case: depending on the EO−surface and water−surface interactions, the space between the perpendicular structures and the surface layer ranges from small to rather large. For a triblock with two hydrophilic tails, neck formation would lead to a high concentration of EO in the contact area of PO-rich cylinders and the PO-rich wetting layer and is entropically unfavorable. Undulation and breaking up into rodlike particles with spherical caps is much more likely. The thickness of this EO/water layer depends, as mentioned before, mainly on the behavior of the water.

Since we have an extra parameter (the water−wall interaction), a complete 3D phase diagram for the three interaction parameters would show very complex, as can be seen from the morphologies in Figures 5 and 6. We have only carried out a sparse sampling of the parameter space, where a full sampling would computationally be impossible. Calculation of one data point roughly takes about a day on a single processor of an SP2 (thin nodes).

In our calculations, we have yet not encountered the surface interaction regions where both E and P wet the surface (the so-called perpendicular region $0.5 < \xi < 0.75$ in the diblock phase diagram). This is the stage where the interaction effects match the entropic effects. To find this region in the triblock case, we performed some extra calculation for $H = 12$ and $\chi_{EM} = \chi_{SM} = 0.2I$ ($I \in \{0, 1, 2, 3, 4\}$) and $\chi_{PM} = 0$. For $I = 5$, the result is $C_{\parallel,1}$ (omitting the P wetting lamellae in this notation); see also Figure 3h.

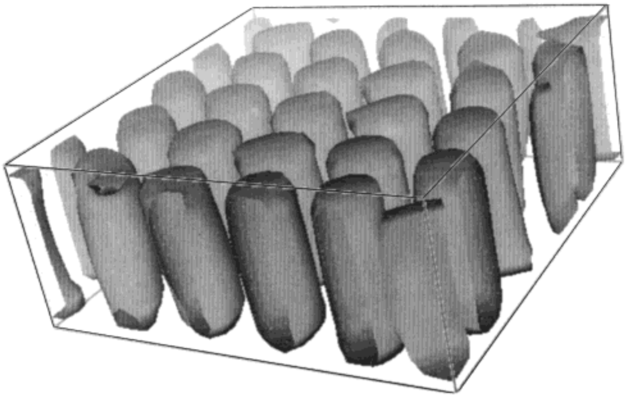

Figure 11. Morphology for $I = 3$ ($\nu\rho_P$ for mean isosurface values) for different hydrophobic surface interaction parameters. Surface interaction parameters for this value of I are $\chi_{EM} = 0.6$, $\chi_{PM} = 0.0$, and $\chi_{ES} = 0.6$. The result is shown for the slit width $H = 12$ and $y = 4000$.

For $I = 0$, 1, and 2 we observe wetting of E and an imperfect $C_{\parallel,2}$ at $y = 4000$. At $I = 3$ there is a hexagonally packed, perfect $C_{\perp}$ phase of P cylinders in an E matrix at the same stage. For $I = 4$, P wetting and a $C_{\parallel,1}$ P phase is observed with some necks to the wetting lamellae. At later time stages ($y = 8000$), these necks are not completely removed, suggesting that this phase point is close to a phase boundary. The orthogonal morphology is depicted in Figure 11. One should note that in this case the cylinders are not influenced by a wetting layer and start at the solid surface.

4. Concluding Remarks

We have used the dynamic density functional method to simulate the behavior of a specific triblock copolymer in a confined environment. The confined geometry is chosen in order to mimic the geometry of a film. The free energy functional includes an extra term which describes interactions of polymer beads with a surface. Time evolution of mesoscopic block copolymer morphologies is studied using time-dependent Landau−Ginzburg equations for the densities of polymer blocks. Noise and compressibility of the system are explicitly taken into account. For the parametrization we have used the fixed values of a previous article.[35] In the simulations, we have considered four different adjustable parameters: the interaction of the different components (EO, PO, and the solvent) with the surfaces and the slit width. We have considered, into reasonable detail, the effect of these three parameters on the (semi)equilibrium morphology that is the result of a dynamic pathway. We have found that some features of asymmetric diblocks without solvents in slits[27] are also present in triblock copolymer films. Because of entropic effects, the short EO part wets the surface most likely in the absence of surface interactions and a stable parallel cylindrical structure is fast obtained for large H. The phase diagram is much alike the phase diagram for asymmetric diblock copolymers as in ref 27 if the EO− and water−wall interactions are treated as a single variable. In the case of slow equilibration, sometimes morphologies follow the path lamellae → perforated lamellae/catenoid phase → cylinders. In some cases, however, frustration leads to perpendicular structures. For the hydrophobic surfaces under consideration, we have, keeping the surface interaction parameters constant, considered the morphologies as a function of slit size *H*. We observe a very regular pattern of layers of parallel cylinders, with intermediate perpendicular orientations when the film thickness is incompatible with a discrete number times the size of the microdomains. Increasing the surface interactions does not remove these intermediate regions. It is shown that by fine-tuning of the surface interaction parameters, in principle many morphology types can be obtained for different slit sizes. For larger slit sizes, the effect is weaker and in general restricted to the layer neighboring the surfaces.

Although it is out of the scope of our current article, several techniques are available to compare our simulation results to experiments. Of these methods, nanotomography[32] looks most promising. Experimental methods, such as AFM with colloidal particles attached to the tip, can be used to obtain necessary parameters for our simulations. A combination of this type of experiments would be a good starting point for the validation of our current findings and will be the subject of future articles.

Acknowledgment. G.J.A.S. acknowledges the support of the MesoDyn project ESPRIT No. EP22685 of the European Community (project finalized February 1, 2000). We thank A. V. Zvelindovksy for helpful remarks. Computer time was provided by the Stichting Nationale Computer Faciliteiten (NCF).

References and Notes

(1) Schmolka, I. R. *Polymers for Controlled Drug Delivery*; CRC Press: Boston, 1991.
(2) Linse, P. *Macromolecules* **1993**, *26*, 4437−4449.
(3) Linse, P. *Macromolecules* **1994**, *27*, 2685−2693.
(4) Linse, P. *Macromolecules* **1994**, *27*, 6404−6417.
(5) Alexandridis, P.; Olsson, U.; Lindmann, B. *Macromolecules* **1995**, *28*, 7700−7710.
(6) Malmsten, M.; Linse, P.; Zhang, K. W. *Macromolecules* **1993**, *26*, 2905−2910.
(7) Linse, P. *J. Phys. Chem.* **1993**, *97*, 13896−13902.
(8) Noolandi, J.; Shi, A. C.; Linse, P. *Macromolecules* **1996**, *29*, 5907−5919.
(9) Tiberg, F.; Malmsten, M.; Linse, P.; Lindman, B. *Langmuir* **1991**, *7*, 2723−2730.
(10) Malmsten, M.; Linse, P.; Cosgrove, T. *Macromolecules* **1992**, *25*, 2474−2481.
(11) Schillén, K.; Claesson, P. M.; Malmsten, M.; Linse, P.; Booth, C. *J. Phys. Chem.* **1997**, *101*, 4238−4252.
(12) Chu, B.; Zhou, Z. In *Nonionic Surfactants. Polyoxyalkylene Block Copolymers*; Marcel Dekker: New York, 1996.
(13) Hamley, I. W. *The Physics of Block Copolymers.*; Oxford University Press: New York, 1998.
(14) van den Berg, R.; de Groot, H.; van Dijk, M. A.; Denley, D. R. *Polymer* **1994**, *35*, 5778−5781.
(15) van Dijk, M. A.; van den Berg, R. *Macromolecules* **1995**, *28*, 6773−6778.
(16) Annis, B. K.; Schwark, D. W.; Reffner, J. R.; Thomas, E. L.; Wunderlich, B. *Makromol. Chem.* **1992**, *193*, 2589−2604.
(17) Foster, M. D.; Sikka, M.; Singh, N.; Bates, F. S.; Satija, S. K.; Majkrzak, C. F. *J. Chem. Phys.* **1992**, *96*, 8605−8615.
(18) Morkved, T. L.; Lu, M.; Urbas, A. M.; Ehrichs, E. E.; Jaeger, H. M.; Mansky, P.; Russell, T. P. *Science* **1996**, *273*, 931−933.
(19) Karim, A.; Singh, N.; Sikka, M.; Bates, F. S.; Dozier, W. D.; Felcher, G. P. *J. Chem. Phys.* **1994**, *100*, 1620−1629.
(20) Mayes, A. M.; Russell, T. P.; Bassereau, P.; Baker, S. M.; Smith, G. S. *Macromolecules* **1994**, *27*, 749−755.
(21) Mansky, P.; Chaikin, P.; Thomas, E. L. *J. Mater. Sci.* **1995**, *30*, 1987−1992.
(22) Hashimoto, T.; Fujimura, M.; Kawai, H. *Macromolecules* **1980**, *13*, 1660−1669.
(23) Matsen, M. W. *Curr. Opin. Colloid Interface Sci.* **1998**, *3*, 40−47.
(24) Binder, K. *Adv. Polym. Sci.* **1999**, *138*, 1−89.
(25) Liu, Y.; Zhao, W.; Zheng, X.; King, A.; Singh, A.; Rafailovich, M. H.; Sokolov, J.; Dai, K. H.; Kramer, E. J.; Schwarz, S. A.; Gebizlioglu, O.; Sinha, S. K. *Macromolecules* **1994**, *27*, 4000−4010.
(26) Radzilowski, L. H.; Carvalho, B. L.; Thomas, E. L. *J. Polym. Sci., Polym. Phys.* **1996**, *34*, 3081−3093.
(27) Huinink, H. P.; Brokken, J. C. M.; van Dijk, M. A.; Sevink, G. J. A. *J. Chem. Phys.* **2000**, *112*, 2452−2462.
(28) Kim, G.; Libera, M. *Macromolecules* **1998**, *31*, 2569−2577.
(29) de Jeu, W. H.; Lambooy, P.; et al. *J. Phys. II* **1993**, *3*, 139−146.
(30) Elbs, H.; Fukunaga, K.; Stadler, R.; Sauer, G.; Magerle, R.; Krausch, G. *Macromolecules* **1999**, *32*, 1204−1211.
(31) Knoll, A.; Magerle, R.; Krausch, G. Submitted to *Macromolecules.*
(32) Konrad, M.; Knoll, A.; Krausch, G.; Magerle, R. *Macromolecules* **2000**, *33*, 5518−5523.
(33) Fraaije, J. G. E. M.; van Vlimmeren, B. A. C.; Maurits, N. M.; Postma, M.; Evers, O. A.; Hoffmann, C.; Altevogt, P.; Goldbeck-Wood, G. *J. Chem. Phys.* **1996**, *106*, 4260−4269.
(34) Sevink, G. J. A.; Zvelindovsky, A. V.; Van Vlimmeren, B. A. C.; Maurits, N. M.; Fraaije, J. G. E. M. *J. Chem. Phys.* **1999**, *110*, 2250−2256.
(35) van Vlimmeren, B. A. C.; Maurits, N. M.; Zvelindovsky, A. V.; Sevink, G. J. A.; Fraaije, J. G. E. M. *Macromolecules* **1999**, *32*, 646−656.
(36) Zvelindovsky, A. V.; Sevink, G. J. A.; Fraaije, J. G. E. M. *Phys. Rev. E*, in press.
(37) Zvelindovsky, A. V.; van Vlimmeren, B. A. C.; Sevink, G. J. A.; Maurits, N. M.; Fraaije, J. G. E. M. *J. Chem. Phys. (Rapid Commun.)* **1998**, *109*, 8751−8754.
(38) Maurits, N. M.; van Vlimmeren, B. A. C.; Fraaije, J. G. E. M. *Phys. Rev. E* **1997**, *56*, 816−825.
(39) Kodama, H.; Doi, M. *Macromolecules* **1996**, *29*, 2652−2658.
(40) Kodama, H.; Komura, S. *J. Phys. II* **1997**, *7*, 7−14.
(41) van Vlimmeren, B. A. C.; Fraaije, J. G. E. M. *Comput. Phys. Commun.* **1996**, *99*, 21−28.
(42) Michielsen, K.; de Readt, H.; Fraaije, J. G. E. M. *Prog. Theor. Phys. Suppl.* **2000**, *138*, 543−548.
(43) Linse, P.; Hatton, T. A. *Langmuir* **1997**, *13*, 4066−4078.
(44) Krevelen, D. W. *Properties of Polymers, Their Correlation with Chemical Structure; Their Numerical Estimation and Prediction from Additive Group Contribution*, 3rd ed.; Elsevier: Amsterdam, 1990.
(45) Maurits, N. M.; Altevogt, P.; Evers, O. A.; Fraaije, J. G. E. M. *Comput. Polym. Sci.* **1996**, *6*, 1−8.
(46) Maurits, N. M.; Zvelindovsky, A. V.; Fraaije, J. G. E. M. *J. Chem. Phys.* **1998**, *109*, 11032−11042.
(47) Claesson, P. M.; Ederth, T.; Bergeron, V.; Rutland, M. W. *Adv. Colloid Interface Sci.* **1996**, *63*, 119−183.
(48) Blomberg, E.; Claesson, P. M.; Warnheim, T. *Colloids Surf., A* **1999**, *159*, 149−157.

MA001378K